

PAPER

Volume and surface loss of O(³P) atoms in O₂ RF discharge in quartz tube at intermediate pressures (10–100 Torr)

To cite this article: A V Volynets *et al* 2019 *J. Phys. D: Appl. Phys.* **52** 395203

View the [article online](#) for updates and enhancements.



IOP | ebooks™

Bringing you innovative digital publishing with leading voices to create your essential collection of books in STEM research.

Start exploring the collection - download the first chapter of every title for free.

Volume and surface loss of O(³P) atoms in O₂ RF discharge in quartz tube at intermediate pressures (10–100 Torr)

A V Volynets[✉], D V Lopaev[✉], S M Zyryanov[✉], M A Bogdanova[✉]
and A T Rakhimov[✉]

Skobeltsyn Institute of Nuclear Physics, Lomonosov State University, Moscow, Russia

E-mail: volynets.sinp.msu@gmail.com

Received 14 March 2019, revised 23 May 2019

Accepted for publication 11 June 2019

Published 22 July 2019



Abstract

The O(³P) atom loss has been studied in O₂ RF plasma in the quartz tube in the intermediate pressure range (10–100 Torr) when the transition from the surface to volume loss is observed. Space- and time-resolved actinometry on Ar and Kr atoms was used to study O(³P) atom loss. The research has shown that such a transition actually takes place. However, it was revealed that the gas temperature plays a significant role in this. Gas temperature was measured spectroscopically using the O₂(*b*¹Σ_g⁺, *v* = 0) → O₂(*X*³Σ_g⁻, *v* = 0) band emission. It was demonstrated that the gas temperature in the plasma volume was rather high (>1200 K) due to the high values of the specific input RF power which in turn led to a significant O(³P) loss rate decrease in the discharge volume. The atomic oxygen loss is limited by the O(³P) surface recombination as well as by the volume recombination in a thin layer near the wall. It leads to a low integral loss rate and provides a high oxygen dissociation degree. Analysis based on measured [O(³P)]/N, *T*_{gas}, O₃ spatial profiles and surface loss model including recombination with chemisorbed and physisorbed atoms has revealed the importance of both surface and volume losses. High values of the specific input RF power also lead to increase of the gas temperature near the wall and the temperature of the internal tube surface. As a result, the O atom surface loss rate increases and the volume loss rate near the wall decreases, so overall the contributions of both O(³P) volume and surface recombination are comparable at pressures up to 100 Torr. The O(³P) loss kinetics at intermediate pressures appears to be a rather complex phenomenon and requires at least 1D or even 2D modeling for its correct description. Using global models under similar conditions may lead to dubious results in a detailed study of kinetic mechanisms and processes, but it can be useful for a simple analysis of experimental results.

Keywords: RF discharge, intermediate pressures, oxygen plasma, atomic oxygen kinetics, optical diagnostics of plasma

(Some figures may appear in colour only in the online journal)

1. Introduction

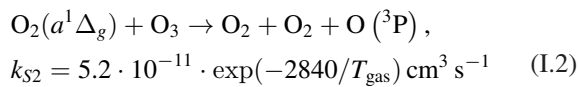
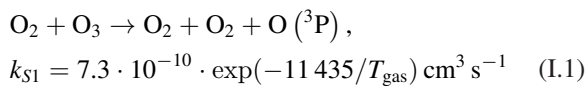
Oxygen plasma is one of most popular objects in applied research, first of all, because of the simplicity of generating large amounts of atomic oxygen which is chemically active in respect to many substances. However, at the same time there are many materials that are inert and do not react with oxygen

atoms under typical plasma conditions. Obvious examples of such materials are dielectrics, for example, glasses and, above all, SiO₂-based ones. Therefore, the use of the glass discharge tubes and chambers just allow generating high O atom concentrations in a volume as well as high O atom fluxes on a surface.

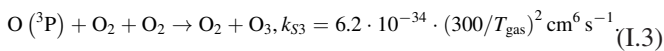
It is obvious that concentration of O atoms in long discharges and continuous wave (CW) plasmas depends both on

O atom production rate, i.e. O₂ dissociation rate, and on the atom loss rate. However, if the O₂ dissociation rate is strictly determined by the plasma parameters and can be estimated using some adequate model parameters, the loss rate can be notably varied depending on conditions such as mixture composition or wall material and surface state. Therefore, under the same plasma conditions the O atom density can be highly different in different chambers. Often simply insufficient knowledge of the true loss rate is a major source of uncertainties in the analysis of O atom kinetics and mechanisms of elementary processes with atomic oxygen. At low pressure the main source of the uncertainties is surface, namely, absence of exact knowledge about surface processes with O atoms. Despite that the mechanisms of O(³P) surface recombination are known and have been studied in whole [1–10], application of the mechanisms in each specific case requires exact knowledge of many parameters, such as, for example, desorption and activation energies, densities of active surface sites, steric reaction factors, etc [5–14]. Moreover, these surface characteristics are not constant, but have complex distributions since surface sites are not absolutely the same [3, 15]. In addition, density of the sites occupied by atoms can also be varied with plasma parameters such as, for example, ion energy and flux [16, 17], as well as O atom flux and gas temperature [17]. Chemisorbed atoms having high desorption energy are stable enough and their density may be changed due to bombardment by energetic ions at low pressure when the plasma sheath is collisionless, while density of physisorbed atoms is very sensitive to energy and the flux of O atoms itself. All of it draws a hardly predictable picture of O(³P) loss.

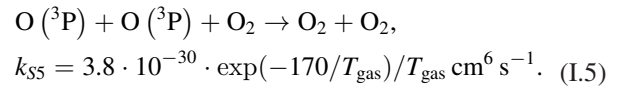
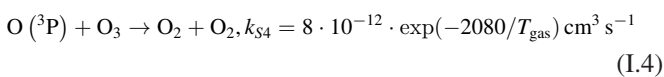
At high pressure, the O(³P) loss is caused by volume reactions leading to O atom transformation into molecular form, O₂ or O₃ with ozone being rather unstable because of low dissociation energy and high reaction ability. In O₂ plasma, there are reactions leading to decay of ozone with reproducing O(³P) atoms, where the most important among them are [18, 19]:



where T_{gas} is gas temperature (measured in K). At temperatures above ~600–800 K (it is very often observed in high-pressure CW discharges) these reactions provide fast decomposition of ozone that may bring to naught the O(³P) loss in the three-body reaction with production of O₃ (reverse reaction to (I.1)) [20]:



The only reactions leading to irreversible loss of O atoms are ones which can provide production of a stable product, i.e. O₂. It is two reactions [21–23]:



All of the above-mentioned processes are temperature dependent; for some processes these dependencies are rather sharp. Therefore, even for not very high gas heating (which is easy reached in high-pressure CW discharges), it is extremely difficult to predict quantitatively spatial behavior of O atoms since temperature spatial distribution appears to be partly a function of the reactions, mainly exothermic ones. The use of 1D–3D models allows one to reproduce it only qualitatively. Therefore, many researchers very often prefer to use direct measurements of O(³P) atoms. Most of them are focused on measuring O(³P) density often with good spatial resolution particularly if one uses laser techniques such as TALIF, similarly to [24–27], for example. However, it is not enough if the aim of research is to study plasma-enhanced mechanisms of elementary reactions with oxygen atoms, for instance. O(³P) density is balanced by the total atom production and loss rates, and it is very important to know (it would be the best to measure) at least one of them.

This work is focused on studying O(³P) atom loss in O₂ plasma in a quartz tube for the case of intermediate pressures ($p \cdot d \sim 10\text{--}100$ Torr cm, where p is pressure and d is the tube diameter) when the transition from the surface to volume losses should occur. The amount of works devoted to this $p \cdot d$ range is rather limited since it is difficult to provide stable homogeneous CW discharge at such conditions because of high gas heating and possible discharge contraction as in case of DC discharges. Therefore, RF high-frequency (81 MHz) discharge was used to generate stable uniform plasma column. The aim of the research was to study the effect of surface and volume loss mechanisms on O(³P) density in intermediate $p \cdot d$ range. The experimental setup is described in section 2. The diagnostic methods used are presented in section 3. The results obtained are shown and discussed in section 4. Finally, the main conclusions of this research are given in section 5.

2. Experimental setup

The experimental setup is shown in figure 1. This research is ideologically similar to the approach of the previous study of nitrogen atoms kinetics [28]. A distinctive feature of this research is use of high-frequency (RF) capacitive discharge in a quartz tube (length—20 cm, inner diameter—1 cm, wall thickness—2 mm) instead of DC as a source in order to obtain long enough stable quasi-uniform plasma column at an elevated pressure range (10–100 Torr). More specifically, transversal CCP discharge with external electrodes along all tube was used. Using CCP coupling allowed removal of the electrodes on the outer side of the discharge tube. As a result, the higher dissociation degrees can be achieved since the loss probability of atomic oxygen on a dielectric (quartz in our case) surface is usually much lower than that on a metal surface [8, 11, 29]. To avoid tube heating and thereby keep the surface conditions approximately the same, the electrodes were cooled by water.

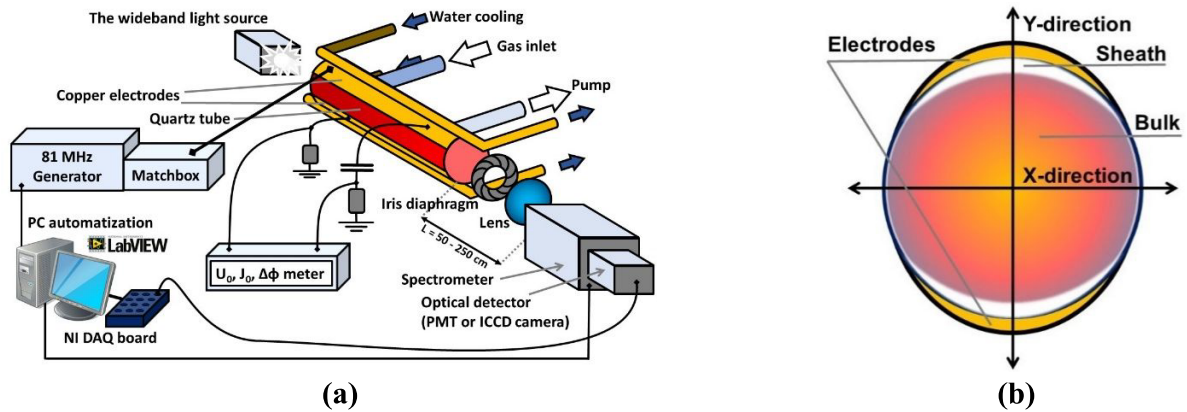


Figure 1. (a) Experimental setup. (b) Front view of the discharge tube. Directions of spatially resolved optical measurements: across the tube center along the electrodes (X) and transverse the electrodes (Y). The electrodes, emission from the plasma sheath (pronounced near the electrodes) and plasma bulk are illustrated.

A sheet made of soft graphite material with high thermal conductivity was inserted between the quartz tube and the copper electrodes to provide better thermal contact.

To apply optical emission and absorption spectroscopy, quartz polished windows were melted to both ends of the quartz tube. Discharge emission from the tube end was passed through an adjustable iris diaphragm and was then focused onto the entrance slit of the imaging spectrometer ('Solar TII MS3504i') that could be combined with various optical detectors. The detector and distance L between the nearest tube window and the slit was chosen depending on diagnostics applied.

The discharge was driven by an 81 MHz electric generator ('Polygon RFPS 500 A81') operating in range 50–500 W. Impedance of electric load was adjusted using an L -type matchbox so that electric power was effectively delivered to the discharge (level of the reflected RF power always did not exceed 1–2 W). However, some part of RF power was dissipated in the matching network. The real values of electric power consumed by the plasma were also estimated experimentally by measuring RF voltage on electrode, RF current and phase shift between them. For that the bottom electrode was connected to the ground via low-inductance 0.061 Ohm shunt resistor. The voltage between the electrodes was obtained using the capacitive divider. Voltage and current were measured directly on a divider and shunt resistor by probes of phase-vector meter 'FK2-12' enabling gating (0.5 ns) measurements in two independent channels in the bandwidth 1–1000 MHz.

The electric generator could be programmed to operate in different modes of power generation: continuous and pulsed (for kinetic studies) with varying power modulation depth. In the latter case, the modulation depth can be varied from 10% up to 100% (i.e. discharge full switching off) with arbitrary choice of modulation frequency (<40 kHz) and the duty cycle.

Pure oxygen was used in this study with small additions of inert gases (no more than 5% in total) for the actinometry technique. For example, the $O_2/Ar/Kr$ mixture used in actinometry contained 2.5% of Ar and 2.5% of Kr. This percent of noble gases almost does not influence discharge parameters since ionization potential of both Ar and Kr is higher

than the O_2 ionization potential that provided approximately the same ion composition (O_2^+ ions) as in pure O_2 . The flow rate of 22 sccm was kept through all the experiments which provided reliable pressure setting in our gas system and ensured residence time of the studied species noticeably longer than the typical lifetimes of all active species in the discharge tube.

Programs created in NI LabVIEW environment and NI DAQ (model 6024E) were actively employed in this research to set and control discharge conditions, scientific equipment, automatize data acquisition and to process the obtained data.

3. Diagnostics

3.1. Gas temperature measurements

The gas temperature T_{gas} was determined using optical emission spectroscopy (OES) by fitting simulated spectra of the $O_2(b^1\Sigma_g^+, v=0) \rightarrow O_2(X^3\Sigma_g^-, v=0)$ band to the measured ones. This method was applied to determine the gas temperature near the tube axis as well as temperature averaged over the tube diameter. Further, with some modification, this method allowed estimation of the radial profiles of $T_{\text{gas}}(r)$.

In the first case, the spectrometer was placed at a relatively short distance ($L \approx 50$ cm), figure 1(a) providing a good signal-to-noise ratio at a reasonable spectral resolution which was enough for temperature measurement (see example in figure 2(a)). ICCD matrix ('DeltaTekh M1400M') was used as an optical detector. The spatial resolution was limited to ~ 1.5 – 2 mm and reached by using the objective together with the iris diaphragm. The narrowest aperture of the diaphragm corresponded to the measurements near the axial region (T_{gas}^a), while the widest aperture was chosen to measure gas temperature averaged over the tube diameter ($\langle T_{\text{gas}} \rangle$). The standard least squares method was used to obtain the T_{gas} value which provides modelled spectrum that best fit the experimental one (the computations were carried out using a special program developed in the LabVIEW environment). Typical relative error (i.e. $\Delta T_{\text{gas}}/T_{\text{gas}}$) estimated by this method was about 5%. Such an approach has been widely used for plasmas of diatomic gases, and the OES method applied here with

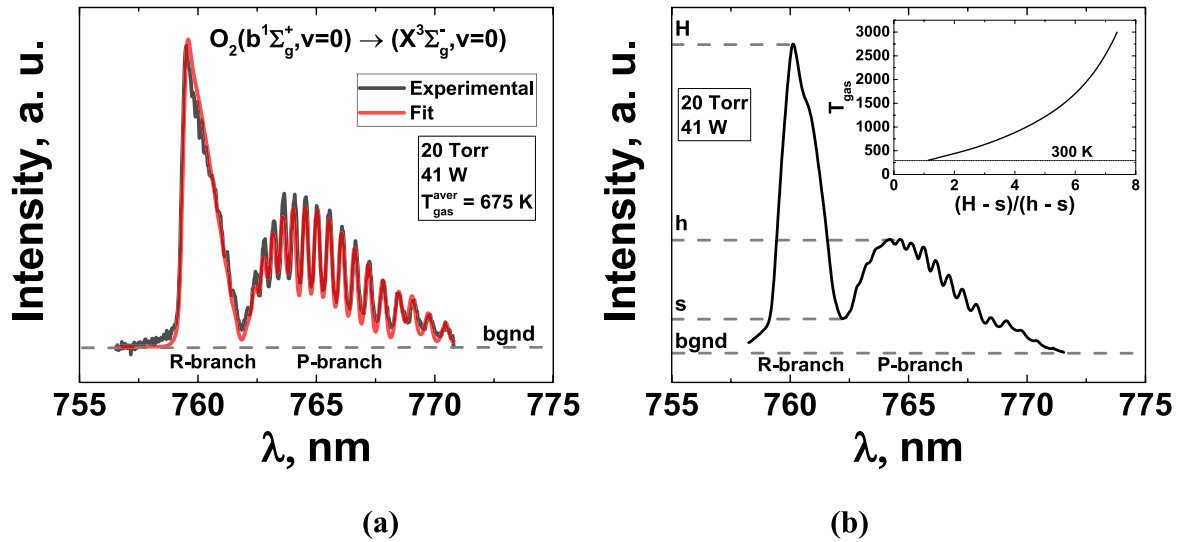


Figure 2. Examples of $O_2(b^1\Sigma_g^+, v=0) \rightarrow O_2(X^3\Sigma_g^-, v=0)$ band emission spectrum at 20 Torr and 41 W input RF power for cases of high resolution (a) and low resolution (b).

$O_2(b^1\Sigma_g^+, v=0) \rightarrow O_2(X^3\Sigma_g^-, v=0)$ band is thoroughly described in [17, 30–32]. Here it should only be mentioned that the shape of the instrumental function of optical system (spectrometer + matrix) is important for correct computation of the spectrum because of inevitable imperfections of the grating and scattering inside different ICCD elements. Therefore, the instrumental function used in the computations was experimentally obtained using a He–Ne laser line. Data on T_{gas}^a and $\langle T_{\text{gas}} \rangle$ obtained in this way are shown below in figure 9 and discussed in section 4.1.

Radial profiles of gas temperature were obtained also using the spectra of $O_2(b^1\Sigma_g^+, v=0) \rightarrow O_2(X^3\Sigma_g^-, v=0)$ but of low resolution over wavelength (see figure 2(b)). A more detailed description of this method can be found in [30, 31]. The idea behind the method is well known. The spectral resolution of the spectrometer is chosen considering that it would be much wider than the spectral distance between lines in one of the branches (R-branch here) and comparable with the same distance in another branch (P-branch here). Hence, the ratio between maximum intensities of the branches becomes rather smooth function of gas temperature. This function depends also on spectrometer resolution. Thus, the shape of low-resolution spectrum can be defined by H , h and s as it is illustrated in figure 2(b). Here H , h and s are intensities which were measured experimentally. The inset in the figure shows the calculated calibration curve $T_{\text{gas}} = f(x)$, where $x = \frac{H-s}{h-s}$ was used to recalculate experimentally measured radial profile into the $T_{\text{gas}}(r)$. To achieve the high spatial resolution (~ 0.2 – 0.3 mm) required in this case, the spectrometer was placed far enough (~ 2.5 m) from the exit window of the tube. A long focus lens was used to provide a sharp image of both windows on the entrance slit. Due to the rather intensive emission from the plasma sheath region near the electrodes, the observation was carried out in the horizontal plane only, i.e. in the ‘X direction’ (as illustrated in figure 1(b)). A dove prism was used to rotate the discharge image from the ‘Y’ to ‘X’ direction.

Examples of the radial profiles $T_{\text{gas}}(r)$ are shown in figure 3. At the higher pressure (60 Torr, figure 3(b)) the $T_{\text{gas}}(r)$ profiles are rather noisy owing to the very low intensity of the $O_2(b^1\Sigma_g^+, v=0) \rightarrow O_2(X^3\Sigma_g^-, v=0)$ band and increased level of the background emission. Nevertheless, these data allowed making adequate estimations of $T_{\text{gas}}(r)$. Since the $T_{\text{gas}}(r)$ profile should be smooth for the studied conditions (low enough $p \cdot d$ at relatively uniform power input), the parabolic fits were used to estimate the true profiles. The error arising in that approximation is quite reasonable and comparable with a data scatter for T_{gas}^a and $\langle T_{\text{gas}} \rangle$.

3.2. Actinometry

Kinetics of oxygen atoms was studied using the actinometry technique. It is well known that actinometry allows evaluating the density of atoms in respect to the density of stable, as a rule, inert gas (actinometer) which is added to the gas in a negligible amount in order not to disturb the plasma. In the given experiment krypton and argon were used as an actinometer. However, since experiments were conducted at high pressures, electron temperature and corresponding effective electric field in plasma bulk were low enough. Therefore, most of the actinometric measurements were done with krypton because the difference between excitation energies for the O and Kr emitting levels chosen for actinometry is smaller (< 1 eV) than the electron temperature T_e , providing a weak dependence on discharge parameters. At the same time, the difference between excitation energies for Ar and Kr emitting levels is slightly higher than T_e . Therefore, the ratio of Ar and Kr spectral line intensities is sensitive to the T_e changes since they hardly depend on the atom densities. Despite the high RF frequency of 81 MHz, electrons undergo few collisions during the RF period because of high pressure that assumes local effective reduced electric field E/N_{eff} . Thus, the ratio $I^{\text{Ar}}/I^{\text{Kr}}$ was used in the study to estimate E/N_{eff} in plasma bulk. The mixture of

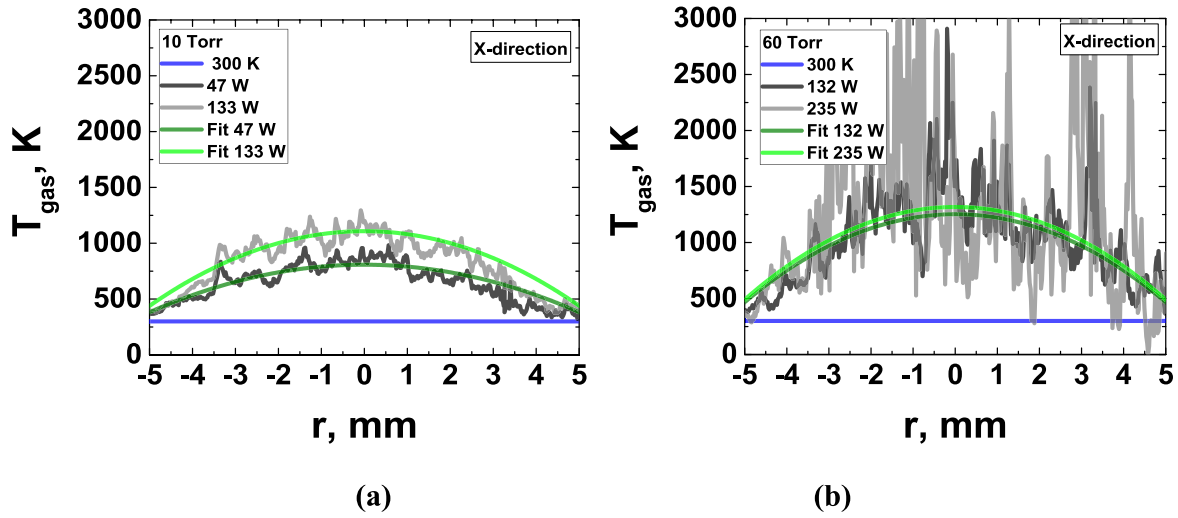


Figure 3. Examples of radial profiles of the gas temperature T_{gas} for 10 Torr (a) and 60 Torr (b) for two values of input RF power.

oxygen with 2.5% Kr and 2.5% Ar was done in advance in a separate balloon for that purpose.

Actinometry was used to study:

1. spatial profiles (along the tube diameter) of O atom mole fraction $[O(^3P)]/N$ and E/N_{eff} at stationary discharge—so-called spatially resolved actinometry and
2. time evolution of $[O(^3P)]/N$ ratio when the input RF power was partially modulated—so-called time-resolved actinometry.

In the present work the following atomic lines were chosen: $O(^5P) \rightarrow O(^5S)$ (777 nm), $Kr(2p_5) \rightarrow Kr(1s_4)$ (758 nm), $Kr(2p_9) \rightarrow Kr(1s_5)$ (811 nm) and $Ar(2p_1) \rightarrow Ar(1s_2)$ (750 nm). The relation between the ratio of O and Kr spectral line intensities ($I_{777}^O/I_{758(811)}^{Kr}$) and the densities of $O(^3P)$ and Kr atoms ($[O(^3P)]/[Kr]$) is given below:

$$\frac{[O(^3P)]}{[Kr]} \cong C_{Kr}^O \cdot \frac{S_{\lambda}^{Kr}}{S_{\lambda}^O} \cdot \frac{I^O}{I^{Kr}}. \quad (1)$$

Here, the term of O_2 dissociation excitation was neglected because of low E/N . C_{Kr}^O is the so-called actinometrical coefficient:

$$C_{Kr}^O = \frac{\sum_j A_{ij}^O + k_q^O \cdot [O_2]}{\sum_m A_{nm}^{Kr} + k_q^{Kr} \cdot [O_2]} \cdot \frac{A_{nm}^{Kr}}{A_{ij}^O} \cdot \frac{k_e^{Kr}}{k_e^O} \quad (2)$$

where A_{ij} are the Einstein coefficients of radiative transition from the i th upper (emitting) state to j th lower state, k_q are quenching rate constants of the upper state through collisions with neutral particles (O_2), S_{ij} is the sensitivity of spectroscopic system at the respective wavelength. Finally, k_e are the excitation rate constants from ground to the upper emitting state by electron impact:

$$k_e = \left(\frac{2e}{m_e}\right)^{1/2} \int_{E_{th}}^{\infty} \sigma_e(\varepsilon) F(\varepsilon) \sqrt{\varepsilon} d\varepsilon, \int_0^{\infty} F(\varepsilon) d\varepsilon = 1 \quad (3)$$

where $\sigma_e(\varepsilon)$ is excitation cross section by electron impact, and $F(\varepsilon)$ is the electron energy distribution function (EEDF).

Designations in the expressions (3) are similar to those used in the paper describing the BOLSIG + software [33].

The Einstein coefficients were taken from the NIST database [34]: $A^{Kr} = 4.31 \cdot 10^7$ 1/s, for 758 nm and $A^{Kr} = 3.6 \cdot 10^7$ 1/s for 811 nm Kr line, $A^O = 4.5 \cdot 10^7$ 1/s for 750 nm Ar line and $A^O = 3.69 \cdot 10^7$ 1/s for 777 nm O line. The concentration of the neutrals was calculated according to the ideal gas law using experimentally measured gas temperatures.

It should be noted that in the elevated pressure range considered here (10–100 Torr) quenching collisions, in fact, determine populations in the upper emitting states. Therefore, exact knowledge of the quenching rate constants is very important for correct measurement of O atom density. However, the values of quenching rate constants are not well-established and sometimes can differ significantly. The most reliable data exist for the quenching rate constant of the excited $O(^3P)$ state (844 nm line) since it was used for TALIF and verified many times [27, 35–37]: k_q^O values are varied approximately from $6 \cdot 10^{-10}$ to $9.5 \cdot 10^{-10}$ $\text{cm}^3 \text{s}^{-1}$ but mostly grouped in the range of $(8.5\text{--}9.3) \cdot 10^{-10}$ $\text{cm}^3 \text{s}^{-1}$. We made a few tests with using both 844 and 777 nm lines for O atom actinometry for different pressures and found that quenching rate constant for the $O(^5P)$ state (777 line) should be slightly (~25%–30%) lower than for the $O(^3P)$ state (844 nm line). Thus, the quenching rate constant for the $O(^5P)$ state (777 line) was taken as $k_q^O = 7 \cdot 10^{-10}$ $\text{cm}^3 \text{s}^{-1}$. The quenching rate constant of $Ar(2p_1)$ was taken from [38, 39]: $k_q^{Ar} = 2.8 \cdot 10^{-10}$ $\text{cm}^3 \text{s}^{-1}$. The quenching rate constant of the $Kr(2p_5)$ and $Kr(2p_9)$ states was estimated by comparing $[O(^3P)]/N$ ratios obtained by actinometry on Kr and Ar atoms: $k_q^{Kr} = 7.6 \cdot 10^{-10}$ $\text{cm}^3 \text{s}^{-1}$. This value is very close to the quenching rate constant of the $Kr(2p_6)$ state often used in TALIF measurements for absolute calibration [35, 40].

The theoretical excitation cross section by electron impact from [41] was used for the $O(^5P)$ state. In amplitude it is close to the well-known cross section [42] but reproduces more accurately the cross section near the excitation threshold. The excitation cross section for the Ar and Kr atomic states were taken respectively from [43, 44].

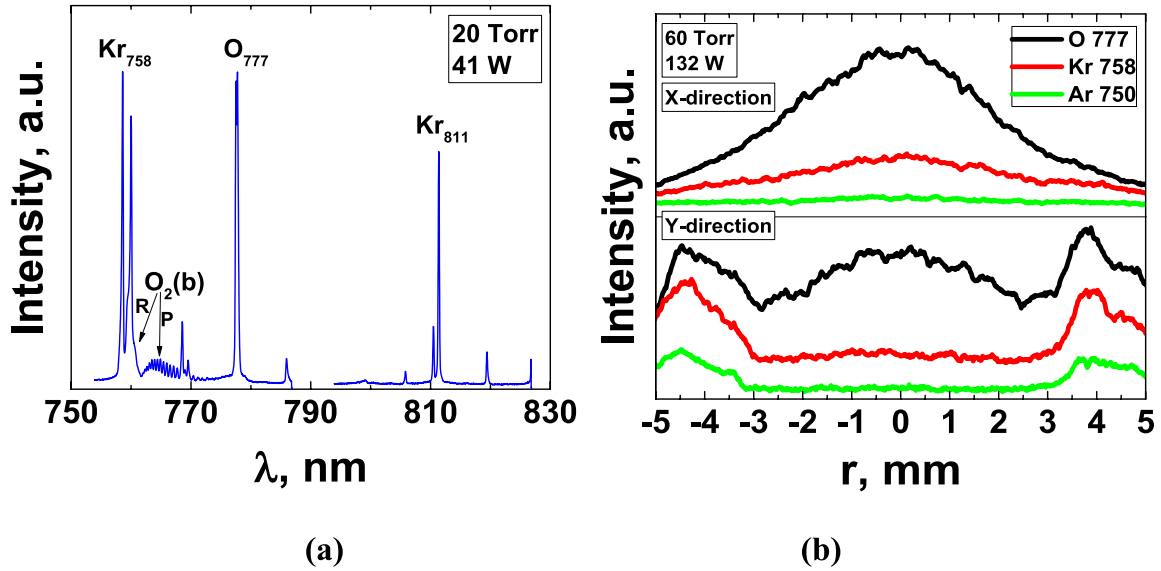


Figure 4. Examples of experimental source data used in the actinometry here. (a) Discharge emission spectra in the area of the oxygen and actinometer spectral lines; (b) radial profiles of the intensities of the optical emission of O, Kr and Ar atoms along the X and Y directions.

Different channels leading to the excitation of the emitting state after electron impact are possible. Besides direct excitation by electron impact, there is also possible excitation due to cascading from the higher states. As a rule, one considers only radiative cascades that are effective only at low pressure (<0.1 Torr). The role of the cascades is different for different states. There are states where cascading excitation is dominant. There are also levels for which the role of cascades is small and sometimes even equal to zero. The apparent cross section just takes it into account. However, at high pressure when collisional quenching prevails over the radiative decay, it is not obvious that quenching will lead to the same cascades. Moreover, if the quencher is the molecule O_2 (like in this study), the quenching of high-energy levels of atoms by molecules very often leads to the excitation transfer into high electronic states of the molecules which mostly are dissociative. This leads to considerable decrease in the role of cascade processes at high pressure. It is also worth noting that direct impact is dominant for all considered atomic levels with the difference between direct and apparent cross section being lower than $\sim 20\%$ – 25% . Thus, we used direct excitation cross sections by electron impact for all the atoms.

As was demonstrated in [45, 46], the actinometric coefficient almost does not depend on the EEDF shape. It occurs due to the fact that this coefficient is defined by the ratio of the excitation rate constants but not the rate constants themselves that can vary very significantly with the EEDF shape at the same time. It allows employing BOLSIG+ software [33] for EEDF calculation instead of full modeling of the discharge. Consequently, for high pressures, when EEDF is local, actinometric coefficient as a function of E/N can be obtained this way (E/N varied from 10 to 200 Td for the considered conditions).

Furthermore, when the excitation energies of the studied specie and actinometer are close enough and their difference is less than electron temperature: $E_{th}^O - E_{th}^{Kr} \ll T_e$ (where

electron temperature T_e can be understood just as mean electron energy for non-Maxwellian cases), the actinometric coefficient also weakly depends on T_e itself. This condition is valid for the levels of O and Kr atoms used. It enables one to minimize the effect of E/N spatial profiles on the O atom mole fraction profiles $[O(^3P)]/N$.

Nevertheless, this effect was also taken into account to reproduce the $[O(^3P)]/N$ profiles most accurately. The spatial profiles of effective E/N_{eff} were estimated by using actinometry of Kr on Ar, since the mole fractions of Ar and Kr atoms are constant and the changes of actinometric coefficient C_{Ar}^{Kr} appear to be connected just with the changes of E/N_{eff} :

$$C_{Kr}^{Ar} \left(\frac{E}{N} \right) \cong \frac{S_{\lambda}^{Ar} I^{Kr}}{S_{\lambda}^{Kr} I^{Ar}}. \quad (4)$$

Here it is taken into account that $[Ar] = [Kr]$.

To implement the space-resolved actinometry, a spectrometer was placed far (~ 2.5 m) from the exit window of the tube. A quartz objective with a diaphragm allowed us to obtain a clear and sharp image of both tube windows at the entrance slit. It provided satisfactory spatial resolution (~ 0.3 mm) that was directly estimated from the difference in the size of windows on images. The ICCD matrix ('DeltaTekh M1400M') was used as an optical detector. Observations were conducted in both the horizontal (X) and vertical (i.e. electrode-electrode, Y) directions (see figure 1(b) for illustration). The Dove prism was used to rotate the image from the (Y) to the (X) direction.

Example of observed spectra for the O_2/Kr (5% Kr) mixture is shown in figure 4(a). The Kr and O spectral lines as well as emission of the $O_2(b^1\Sigma_g^+, v=0) \rightarrow O_2(X^3\Sigma_g^-, v=0)$ band are clearly seen. The typical profiles of O, Kr and Ar spectral line intensities are presented in figure 4(b). It is clearly seen that the vertical (Y) profiles are highly modified near the electrode sheath area because of the influence of high electric fields there.

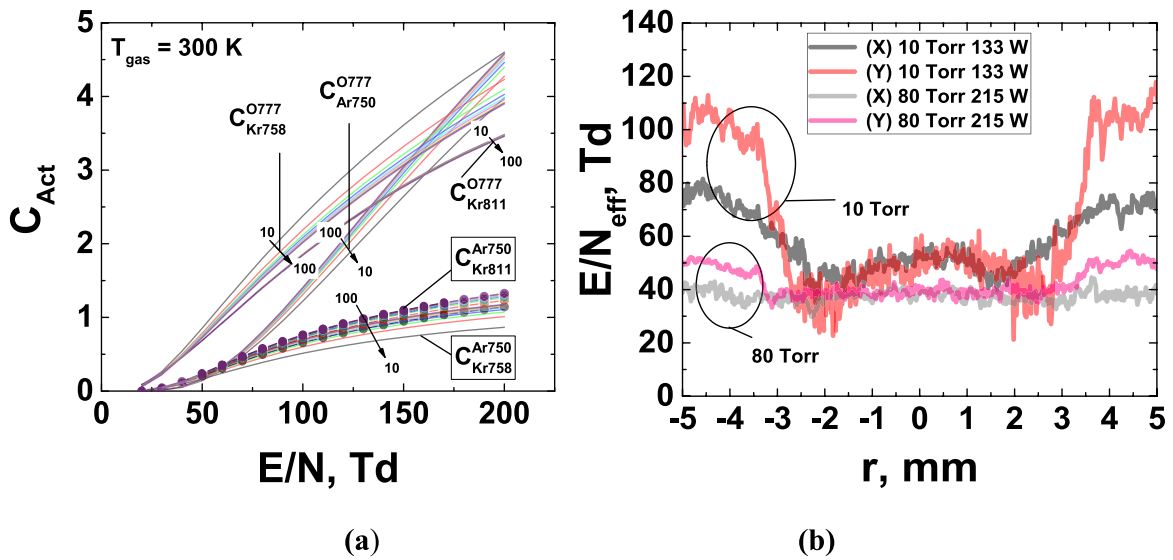


Figure 5. (a) Actinometrical coefficients for atomic lines versus the reduced electric field E/N_{eff} for pressures from 10 to 100 Torr with a step of 10 Torr. Arrows with numbers show the direction of the pressure growth. The $C_{\text{Kr}}^{\text{Ar}}$ coefficients (shown in the black frame) were used to estimate E/N_{eff} radial profiles. (b) Examples of E/N_{eff} radial profiles along the vertical (Y) and horizontal (X) directions at low (10 Torr) and high (80 Torr) pressures.

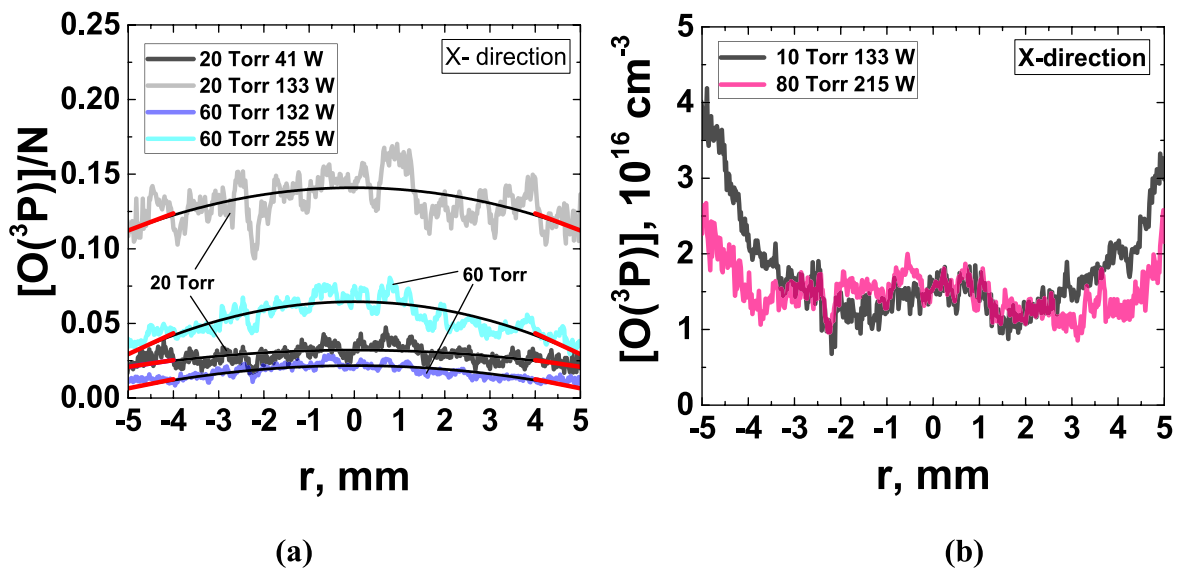


Figure 6. Examples of measured radial profiles of $[\text{O}^3\text{P}]/N$ ratio (a) and estimated $[\text{O}^3\text{P}]$ density (b) at 10 Torr and 60 Torr. Values of the input RF power in each case are indicated on the graphs. Red thick lines illustrate the gradients of $[\text{O}^3\text{P}]/N$ profiles near the wall.

The calculated actinometric coefficients C_{Kr}^{O} , C_{Ar}^{O} and $C_{\text{Ar}}^{\text{Kr}}$ are shown in figure 5(a) and are a function of reduced electric field E/N_{eff} for different pressures. Examples of the E/N_{eff} profiles obtained using (4) are shown in figure 5(b). As can be seen, E/N_{eff} changes only slightly in the plasma bulk in different regimes. However, near the electrodes the E/N_{eff} notably grows with increasing RF power, but this growth reduces with increasing pressure. In the (X) direction, the E/N_{eff} changes in the plasma sheath near the wall are rather small so that one would expect small E/N influence on the $[\text{O}^3\text{P}]/N$ profiles. How much so is discussed below, in section 4.4. Thus, only horizontal (X) profiles were considered further to avoid the distortions owing to the high electric fields in the near-electrode area.

The examples of $[\text{O}^3\text{P}]/N$ profiles are presented in figure 6(a). It is seen that $[\text{O}^3\text{P}]/N$ profiles are concave, indicating O^3P loss in the wall area. As discussed further (section 4.4), near-wall gradients of the $[\text{O}^3\text{P}]/N$ profiles can be directly connected with the characteristic loss time of oxygen atoms $\tau_{\text{Loss}}^{\text{O}}$. These gradients are illustrated by short red lines.

An example of $[\text{O}^3\text{P}]$ density profiles estimated from the $[\text{O}^3\text{P}]/N$ and gas temperature profiles using ideal gas law is shown in figure 6(b). The $[\text{O}^3\text{P}]$ profiles were used to analyze mechanism of O^3P atom loss (see section 4). Overall, the accuracy of absolute measurements of O^3P atom density is determined by uncertainties of absolute measurements of both $[\text{O}^3\text{P}]/N$ and T_{gas} . We estimated that uncertainties of the absolute $[\text{O}^3\text{P}]/N$ measurements are higher since they

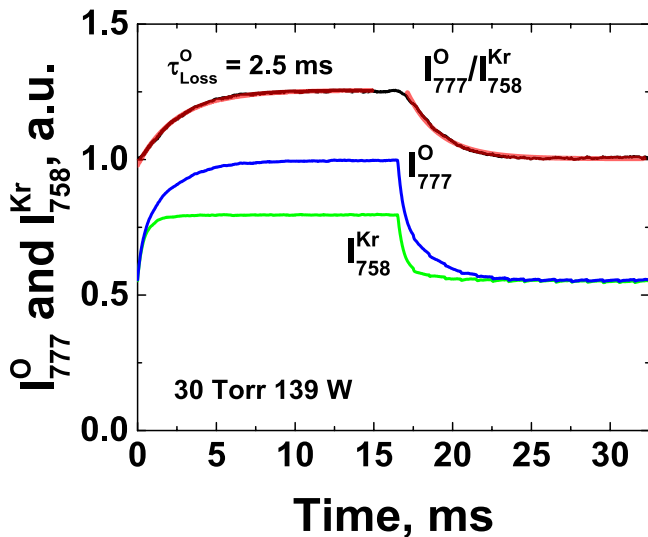


Figure 7. Time-resolved actinometry: example of dynamics of O and Kr emission intensities (I_{777}^O and I_{758}^{Kr}) and their ratio I_{777}^O/I_{758}^{Kr} during RF power partial modulation. Red curves are the exponential fits of the $I_{777}^O/I_{758}^{Kr}(t)$ growth and decay with characteristic loss time τ_{Loss}^O .

include uncertainties of the cross sections, quenching rate constants and EEDF (E/N_{eff}). Therefore, it is rather difficult to estimate the uncertainties of actinometry. But following results of [45], one can estimate the error of the absolute actinometric measurements as $\pm 30\%$ – 40% .

As in [11, 17, 47], time-resolved actinometry was applied to measure the total loss rate of oxygen atoms $\nu_{Loss}^O = (\tau_{Loss}^O)^{-1}$, i.e. including both surface and volume processes. For that purpose, the generator was programmed to operate at partial modulation of $\sim 10\%$ of nominal power. The characteristic rise and fall times of the modulation were $\sim 2 \mu s$. The spectrometer was switched to monochromator mode, and the PMT was used as an optical detector. The diaphragm was adjusted to collect emission only from the axial area of the plasma column excluding plasma sheaths in order to provide applicability of actinometry.

During the experiments, the dynamics of intensities of the atomic spectral lines, 777 nm of O and 758 nm of Kr, was observed: for example, those of $I_{777}^O(t)$ and $I_{758}^{Kr}(t)$ as well as their ratio $I_{777}^O/I_{758}^{Kr}(t)$ are shown in figure 7. Rise and fall dynamics of I_{777}^O/I_{758}^{Kr} demonstrates behavior close to the exponential despite that the intensity of krypton line does not change as abruptly as the RF power. $I_{758}^{Kr}(t)$ changes slower due to slower build/decay of electron density n_e and gas temperature T_{gas} . Intensity of oxygen atoms also responds to these changes as well as to changes in O atom density. However, since the effective reduced field E/N_{eff} almost does not change during the partial modulation, the actinometric coefficient C_{Kr}^O also almost does not change. Therefore, as shown in [17, 47], the ratio $I_{777}^O/I_{758}^{Kr}(t)$ directly corresponds to the dynamics of $O(^3P)$ atom mole fraction $[O(^3P)]/N$ excluding maybe only a very small time < 0.1 ms after discharge power switching. Since $I_{777}^O/I_{758}^{Kr}(t)$ can be fitted rather well by the exponential function, the exponential fit allows us to obtain the total loss time of oxygen atoms τ_{Loss}^O .

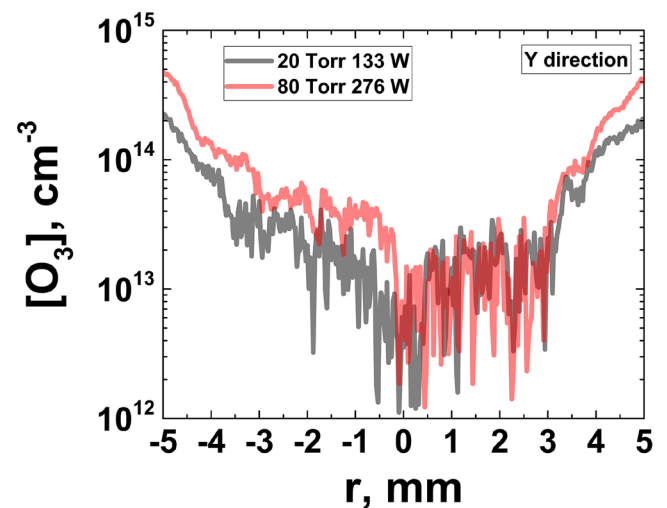


Figure 8. Examples of ozone density radial profiles.

3.3. UV absorption spectroscopy

UV absorption spectroscopy of O_3 Hartley band was applied to study the radial distribution of ozone in the discharge tube. An ultrabright high-stable laser-driven Xe lamp (‘ISTEQ XWS-65’) was used as a source of wideband UV emission. Since the emitting Xe plasma is generated only in the laser focus, the size of the light source is rather small, $\sim 300 \mu m$ in diameter. Thus, the use of parabolic mirror (‘Edmund Optics’) and the iris diaphragm allowed the forming of a beam of almost parallel rays passing through the tube. This beam fell then on the entrance slit of spectrometer where ICCD matrix (‘DeltaTekh M1400M’) was employed as an optical detector. This setup is illustrated in figure 1(a).

To measure radial profiles of ozone density, the absorption of optical emission by the plasma was measured at two wavelengths corresponding to the maximum and edge of the Hartley band ($\lambda_{max} \approx 260$ nm and $\lambda_{edge} \approx 280$ nm) [48, 49]. The difference of the absorption cross sections for these wavelengths is $\sim 10^{-17} \text{ cm}^2$ [49]. The diagnostic was organized this way because some distortion of the light beam (not related to ozone molecules) was also observed. Some possible sources of such distortion include heating of the gas and optical windows which operate similarly to long-focus lenses changing light intensity on the spectrometer slit at different temperatures. Therefore, this differential approach was used to exclude such effects.

Examples of the ozone profiles obtained are shown in figure 8. The profiles near the tube center are very noisy due to the low O_3 concentration (close to the sensitivity limit of the detecting system used). It can be well seen that ozone is concentrated near the cold wall, and in the central region the O_3 concentration is almost an order of magnitude less than near the walls. The $[O_3]$ profile is not a reverse copy of gas temperature profile: it is sharper, indicating a O_3 positive gradient to the tube axis. It means that ozone is mainly produced near the wall and on the surface [50–52] while lost in the volume. Indeed, at the high temperatures observed, ozone molecules should dissociate very fast in the central region and, therefore, only near the relatively cool walls does the thin ozone ‘peel’

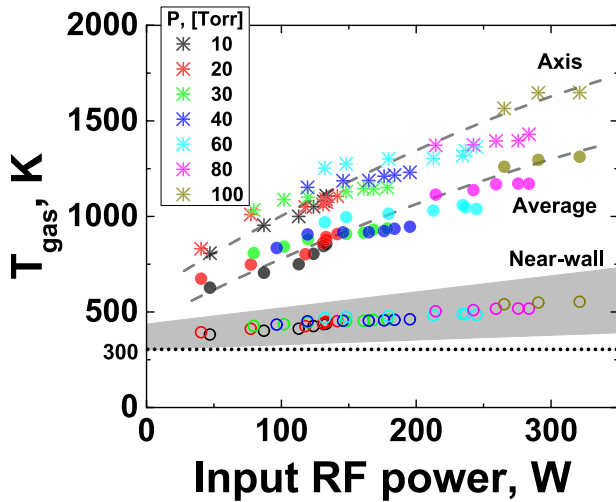


Figure 9. Gas temperature at the tube axis (T_{g_axis}), averaged over the tube cross section (T_{g_aver}) and near the wall (T_{g_nw}) as a function of input RF power at different pressures. T_{g_axis} and T_{g_aver} data were obtained by fitting simulated spectrum of $O_2(b^1\Sigma_g^+, v=0) \rightarrow O_2(X^3\Sigma_g^-, v=0)$ band to the measured one. Data for T_{g_nw} were obtained by using the relation between T_{g_nw} and T_{g_aver} from [17]. The grey field shows schematically a scatter of the T_{g_nw} data extracted from radial profiles $T_{gas}(r)$.

remain. These results are important for estimation of volume losses of O atoms and are discussed further in section 4.4.

4. Results and discussion

4.1. Gas and wall temperatures

Gas temperature averaged over the tube cross section as well as gas temperature at the tube axis are shown in figure 9 as a function of the input RF power at different pressures. Data for different pressures almost fall into one curve so that the gas temperature is only some smooth function of the RF power input, not pressure. This is an expectable result since in the studied conditions the O_2 thermal conductivity has very little dependence on pressure. It can be seen that the gas is heated to rather high temperatures above 1000 K due to high values of specific input RF power. This induces different important effects that will be discussed below. One of the effects is high enough gas heating near the wall because of the non-zero accommodation coefficient α for SiO_2 -based glasses. Recently in [17] it was demonstrated that for Pyrex, α is ~ 0.3 .

We tried to use the measured radial profiles $T_{gas}(r)$ to estimate gas temperature near the wall T_{g_nw} as a function of the input RF power. However, scatter in T_{g_nw} appeared to be rather large and did not allow making a rigorous conclusion about T_{g_nw} behavior and thereby indirectly about the value of the accommodation coefficient α . Therefore, we assumed and used the same accommodation coefficient $\alpha \approx 0.3$ and the same relation between average gas temperature and temperature near the wall as in [17]: $T_{g_nw} \approx 0.28 \cdot (T_{g_aver} - T_w) + T_w$, where T_w is temperature of the internal surface of the tube. Compared to [17], the power density dissipated on 1 cm^2 of the wall is not negligible and can lead to a heating of the

internal surface of the tube despite effective cooling of the external surface. Using the known thermal conductivity of quartz and thickness of the tube wall (2 mm), we estimated T_w as a function of input RF power: $T_w[\text{K}] \approx 300 + \text{Power}[\text{W}]/5$. With these suggestions the T_{g_nw} values fall approximately in the middle of the scatter of $T_{g_nw_R}$ (gray field in figure 9) estimated from the radial profiles, i.e. it looks like the root-mean-square approximation of the $T_{g_nw_R}$ data.

4.2. O atom density

Actinometric measurements of $[O(^3P)]/N$ were carried out along both the Y and X directions. The results are presented in figure 10(a), where $[O(^3P)]/N$ ratio is shown as a function of input RF power for different pressures. As can be seen, $[O(^3P)]/N$ values for both directions are close. It indirectly confirms the applicability of the actinometry technique for correct estimation of $[O(^3P)]/N$ in the conditions studied. Due to high specific power input leading to high plasma density, the $[O(^3P)]/N$ ratio reaches a rather high value, above 20% for 10 Torr, but gradually decreases with increasing pressure. It provides high $O(^3P)$ atom density as well as high $O(^3P)$ flux toward the wall at all pressures.

The $O(^3P)$ atom densities near the wall ($[O(^3P)]_{nw}$) were estimated by using the $[O(^3P)]/N$ radial profiles and the gas temperatures near the wall (T_{g_nw}). The results are shown in figure 10(b) for different pressures as a function of input RF power. The $[O(^3P)]_{nw}$ density is saturated with increasing power and even slightly decreases with the pressure growth. It indirectly indicates there is some fast process that limits the oxygen atom density growth with pressure and RF power and this process considerably contributes to the $O(^3P)$ density balance. In other words, the $O(^3P)$ losses should be increased notably with both pressure and RF power. In the considered conditions oxygen atoms can be lost both on the wall and in the volume.

4.3. O atom surface loss

To estimate surface loss of $O(^3P)$ atoms, we applied the developed recently model [17] of recombination of oxygen atoms on a Pyrex surface in conditions of pure O_2 plasma since Pyrex is also a SiO_2 -based material like quartz. In [17] it was shown that at surface temperatures above room temperature the $O(^3P)$ atom surface recombination proceeds according to Eley-Rideal mechanism when $O(^3P)$ atom from a gas phase can directly recombine with both chemisorbed and physisorbed atoms due to high O atom flux from the plasma to the surface. It was also shown that the recombination is activated not only by surface temperature but also by temperature (energy) of $O(^3P)$ atoms coming from the gas phase. Therefore, the gas temperature near the wall T_{g_nw} is also one of the key parameters of ER recombination. Since in our experimental conditions of high specific RF powers the gas temperature near the wall is not negligible, we used the above-mentioned model. In addition, we also tried to account for the effect of surface temperature T_w since the heating of the internal surface of the

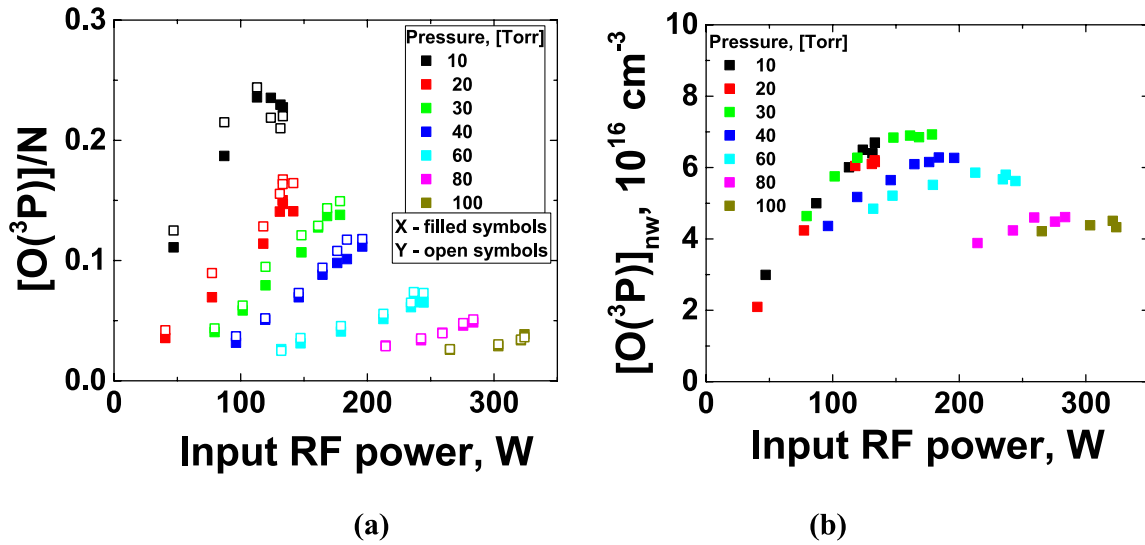
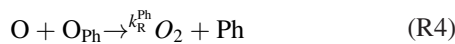
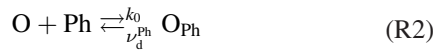


Figure 10. $[O(^3P)]/N$ ratio (a) and $O(^3P)$ atom density near the wall— $[O(^3P)]_{nw}$ (b) as function of input RF power at different pressures.

tube under the considered conditions can influence desorption of weakly bonded physisorbed atoms.

Similarly to [17] we considered two types of active surface sites where O atoms can be adsorbed: chemisorption sites with ‘strongly bonded’ O atoms so that the atom desorption rate from these sites can be neglected compared to the adsorption rate (irreversible adsorption), and physisorption sites with ‘weakly bonded’ atoms whose surface density is ruled just by desorption rate since it is comparable and can be higher than the adsorption rate. Thus, such a model is simple enough and includes only four processes:



where O_{Ch} (O_{Ph}) and Ch (Ph) represent a chemisorbed (physisorbed) atom and a free chemisorption (physisorption) site respectively. Process (R2) describes adsorption/desorption balance. Processes (R3) and (R4) correspond to $O(^3P)$ atom recombination with a chemisorbed and physisorbed atom, respectively. Almost all chemisorption sites are occupied by O atoms. Thus, $[O_{Ch}] \gg [Ch]$ and $[O_{Ch}] \approx [Ch_0]$ ($[Ch_0] \approx 10^{14} \text{ cm}^{-3}$ for SiO_2 -based glasses [6, 8, 14, 15, 17]). It is valid even for rather low O atom densities as $\sim 10^{12}$ – 10^{13} cm^{-3} [6, 12]. For the experimental conditions studied here the $O(^3P)$ density is higher by two orders of magnitude at least. The main difference from the recombination involving chemisorption sites is that the surface density of physisorbed atoms is determined by an adsorption/desorption equilibrium because the desorption energy is low enough and promotes fast depopulation of most of the sites above room temperature [8, 9].

The desorption rate from physisorption sites, ν_d^{Ph} , is given in the simple form:

$$\nu_d^{Ph} = \nu_0 \cdot \exp\left(-\frac{E_d^{Ph}}{kT_w}\right) \quad (5)$$

where $\nu_0 \approx 10^{13} \text{ s}^{-1}$ corresponds to the vibration frequency of particles in the adsorption potential well, T_w is the surface temperature and E_d^{Ph} is the desorption energy for physisorbed O atoms. Due to the high desorption rate at temperatures around room temperature, the surface density of physisorbed atoms under most conditions including the studied conditions is significantly lower than total density of physisorption sites ($[O_{Ph}] \ll [Ph_0]$), and therefore can be found from a sorption equilibrium:

$$[O_{Ph}] = \frac{[O]_{nw}}{O_f} \cdot [Ph], [Ph] = \frac{[Ph_0]}{1 + [O]_{nw}/O_f}, \quad (6)$$

where $[Ph_0] \approx (3\text{--}10) \cdot 10^{15} \text{ cm}^{-2}$ (including the surface roughness factor) is the total density of physisorption sites and $O_f = \nu_d^{Ph}/k_0$ is the gas-phase concentration of $O(^3P)$ atoms necessary to cause occupation of half of the total number of physisorption sites, i.e. $\frac{[Ph]}{[Ph_0]} = 1/2$ when $[O]_{nw} = O_f$. $[O] \ll O_f$ for most of discharge conditions, including those considered here. Thus,

$$[O_{Ph}] \approx \frac{[O]_{nw}}{O_f} \cdot [Ph_0] \text{ and } [O_{Ph}] \ll [Ph_0]. \quad (7)$$

The rate constants for reactions (R3) and (R4), k_R^{Ch} and k_R^{Ph} , are expressed in the usual Arrhenius form,

$$k_R^{Ch} = k_0 \cdot P_0 \cdot \exp\left(-\frac{E_{act}^{Ch}}{kT_{g_nw}}\right) \quad (8)$$

$$k_R^{Ph} = k_0 \cdot P_0 \cdot \exp\left(-\frac{E_{act}^{Ph}}{kT_{g_nw}}\right) \quad (9)$$

where T_{g_nw} is the temperature of the recombining atoms incident on the surface, E_{act}^{Ch} and E_{act}^{Ph} are the activation energies for recombination with chemisorbed and physisorbed

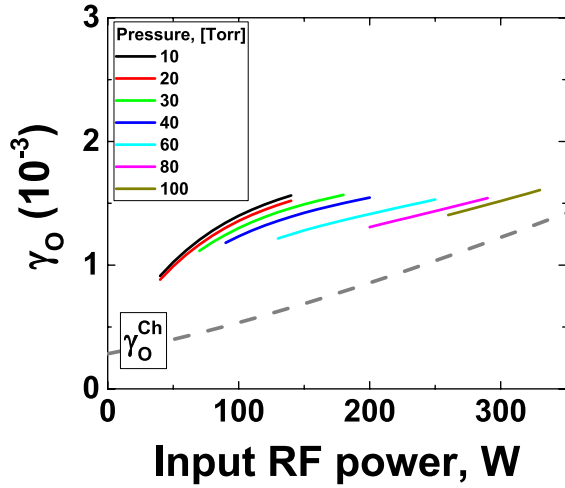


Figure 11. The model results for O(³P) surface loss probability depending on input RF power and gas pressure. The dashed gray line is the loss probability at chemisorbed atoms— $\gamma_{\text{O}}^{\text{Ch}}$.

Table 1. Model parameters used for γ_{O} calculation^a.

Model parameter	$E_{\text{act}}^{\text{Ch}} = E_{\text{act}}^{\text{Ph}}$
Activation energy $E_{\text{act}}^{\text{Ch}} = E_{\text{act}}^{\text{Ph}}$ [eV]; [K]	0.13 (1500 K)
O atom desorption energy E_{d}^{Ph} [eV]; [K]	0.302 (3500 K)
Adsorption rate constant K_0 [$\text{cm}^3 \text{s}^{-1}$]	10^{-10}
Reaction probability P_0	0.044
Chemisorption site density [Ch_0] [cm^{-2}]	$1.5 \cdot 10^{14}$
Physisorption site density [Ph_0] [cm^{-2}]	10^{16}

^a Parameters are the same as in [17].

atoms. P_0 is a reaction probability accounting for the steric and chemical properties of the active sites, and it is often used as a fitting parameter in phenomenological models. Finally, k_0 is rate of collisions of the atoms coming from the gas phase with the adsorbed atoms. One can draw a direct analogy with the gas-phase collision rate constant K_0 , estimating it simply as $K_0 \sim a^2 \cdot v_{\text{th}} \sim 10^{-10} \text{ cm}^3 \text{ s}^{-1}$, where $a \approx 0.25 \text{ nm}$ is the characteristic distance between surface atoms (reflecting characteristic size of the interaction area with adsorbed O atom), v_{th} is thermal velocity of oxygen atoms. Thus, $k_0 \approx K_0^{-1} \cdot S/V$, where S and V are the surface area and the volume of the discharge chamber, respectively.

The flux of atoms undergoing ER recombination with chemisorbed and physisorbed atoms at the surface can be written as

$$k_{\text{R}}^{\text{Ch}} [\text{OCh}] [\text{O}]_{\text{nw}} = \gamma_{\text{O}}^{\text{Ch}} \cdot \frac{[\text{O}]_{\text{nw}} v_{\text{th}}}{4}, k_{\text{R}}^{\text{Ph}} [\text{OPh}] [\text{O}]_{\text{nw}} = \gamma_{\text{O}}^{\text{Ph}} \cdot \frac{[\text{O}]_{\text{nw}} v_{\text{th}}}{4} \quad (10)$$

where $[\text{O}]_{\text{nw}}$ is density of O(³P) atoms near the wall, $\gamma_{\text{O}}^{\text{Ch}}$ and $\gamma_{\text{O}}^{\text{Ph}}$ are the O atom loss probabilities with chemisorbed and physisorbed atoms, respectively. It leads to the following expressions for $\gamma_{\text{O}}^{\text{Ch}}$ and $\gamma_{\text{O}}^{\text{Ph}}$:

$$\gamma_{\text{O}}^{\text{Ch}} \approx \frac{4}{v_{\text{th}}} \frac{2}{R} K_0 P_0 [\text{Ch}_0] \cdot \exp\left(-\frac{E_{\text{act}}^{\text{Ch}}}{kT_{\text{g,nw}}}\right) \quad (11)$$

$$\gamma_{\text{O}}^{\text{Ph}} \approx \frac{4}{v_{\text{th}}} \frac{2}{R} K_0 P_0 [\text{Ph}_0] \cdot \exp\left(-\frac{E_{\text{act}}^{\text{Ph}}}{kT_{\text{g,nw}}}\right) \cdot \frac{[\text{O}]_{\text{nw}}}{\text{O}_f} \quad (12)$$

Finally, the total loss probability given by $\gamma_{\text{O}} = \gamma_{\text{O}}^{\text{Ch}} + \gamma_{\text{O}}^{\text{Ph}}$ is

$$\gamma_{\text{O}} = \gamma_{\text{O}}^{\text{Ch}} \cdot \left(1 + \frac{[\text{Ph}_0]}{[\text{Ch}_0]} \frac{[\text{O}]_{\text{nw}}}{\text{O}_f} \cdot \exp\left(-\frac{E_{\text{act}}^{\text{Ph}} - E_{\text{act}}^{\text{Ch}}}{kT_{\text{g,nw}}}\right)\right) \quad (13)$$

In [17], there were considered two limiting scenarios. In the first one, it has been assumed that the activation energies for ER recombination are the same for chemisorbed and physisorbed O atoms, i.e. $E_{\text{act}}^{\text{Ch}} = E_{\text{act}}^{\text{Ph}}$. In the second scenario, ER recombination with physisorbed atoms is considered to be similar to volume three-body recombination, which has zero activation energy and where the surface plays the role of the third body, i.e. it is assumed that $E_{\text{act}}^{\text{Ph}} = 0$. In [17], it was demonstrated that the difference between two scenarios is not critical despite the first scenario providing values of loss probabilities closer to the experimental data. Therefore, without losing generality, we used the first scenario to estimate the O(³P) surface loss probability. In this case the total γ_{O} is written as

$$\gamma_{\text{O}} \approx \gamma_{\text{O}}^{\text{Ch}} \cdot \left(1 + \frac{[\text{Ph}_0]}{[\text{Ch}_0]} \frac{[\text{O}]_{\text{nw}}}{\text{O}_f}\right) \quad (14)$$

Thus, the O(³P) surface loss probability appeared to be dependent on the discharge parameters through the atom density near the wall $[\text{O}]_{\text{nw}}$ as well as $\gamma_{\text{O}}^{\text{Ch}}$ and O_f which exponentially depend on, respectively, the gas temperature near the wall $T_{\text{g,nw}}$ and the surface temperature T_{w} . All this can explain the change of γ_{O} with discharge power and pressure as well as surface temperature.

Expression (14) was used to calculate the O(³P) surface loss probabilities, γ_{O} , using the measured $[\text{O}(\text{³P})]/N$ ratio as well as estimated $T_{\text{g,nw}}$ and T_{w} . The calculation results are shown in figure 11, while the used parameters are presented in table 1. For generality, values of the model parameters are the same as in [17]. The loss probability at chemisorbed atoms is also shown by the dashed line. It can be seen that γ_{O} gradually increases with the input RF power and pressure. It is partly explained by the increase of $\gamma_{\text{O}}^{\text{Ch}}$ due to increasing $T_{\text{g,nw}}$ with RF power. However, surface recombination with physisorbed atoms also plays an essential role. So, its contribution is greater than 50% at the lowest studied pressures (10 and 20 Torr) due to high O atom flux to the surface ($[\text{O}]_{\text{nw}}$) and low wall temperature (T_{w}). With increasing pressure this contribution is reduced because of the wall temperature increase owing to high input RF power. Thus the γ_{O} values change approximately from 0.001 to 0.002, which correlate well with literature data for similar conditions [5, 7, 8, 11, 17, 53].

4.4. Volume loss

In the considered experiment, the pressure is high enough to provide a contribution of volume processes to the O(³P) loss. However, this contribution greatly depends on the spatial distributions of both reagents and gas temperature since

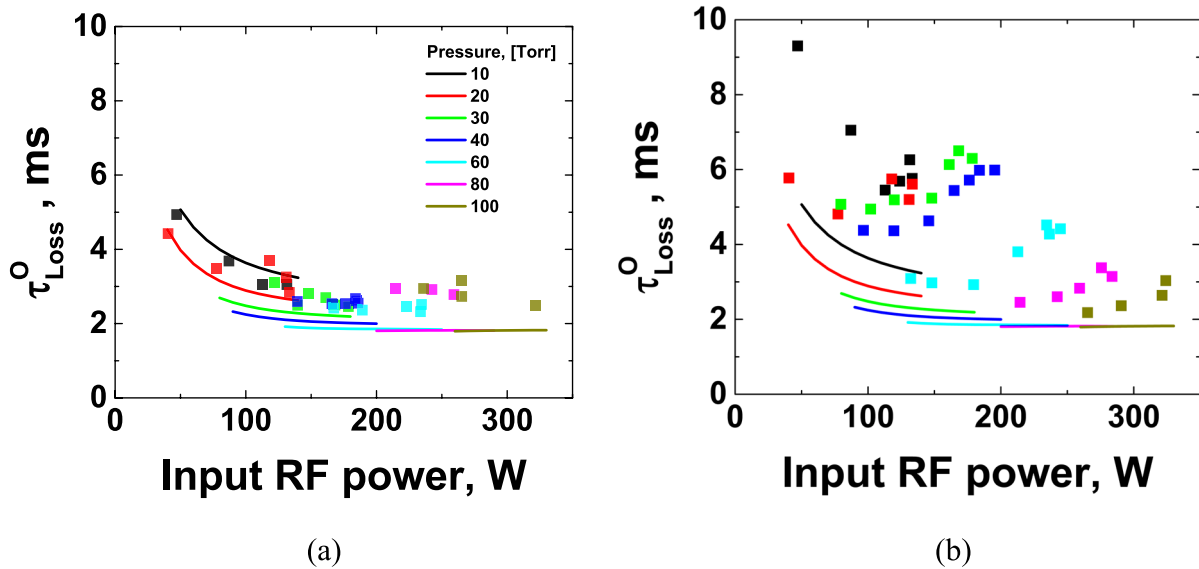


Figure 12. (a) Characteristic loss time of $O(^3P)$ atoms (a) obtained by time-resolved actinometry and (b) estimated from $[O(^3P)]/N$ radial profiles (space-resolved actinometry) as a function of input RF power at different pressures. Symbols—experimental data. Curves—results of the analytical model.

many rate constants of the processes are highly temperature dependent.

The partial RF power modulation ($\sim 10\%$) was used to estimate characteristic loss time of $O(^3P)$ atoms by measuring the dynamics of the corresponding mole fraction ($[O(^3P)]/N$ ratio) using time-resolved actinometry. This is possible owing to the fast establishing time for EEDF and electron density (< 0.1 ms) and since the gas heating/cooling effects can be excluded. Details of this diagnostics were given above in section 3.2. To estimate $O(^3P)$ characteristic loss time and correspondingly the $O(^3P)$ total loss rate, $[O(^3P)]/N$ buildup and decay curves were fitted with exponential functions which correspond to the first-order $O(^3P)$ loss process that is typical for wall loss. As can be seen from example in figure 7 where exponents fit well the $[O(^3P)]/N$ dynamics, the $O(^3P)$ loss can actually be described by such a process to a large extent. Possibly some initial $O(^3P)$ decay goes slightly faster than the exponential fit. But this is not of high value, and the exponential fits allow one to estimate characteristic loss time (τ_{Loss}^O) for $O(^3P)$ atoms quite correctly.

Results of time-resolved actinometry are presented in figure 12(a), where τ_{Loss}^O is shown as a function of input RF power into the plasma at different pressures. It is interesting to note that besides the lowest pressure (10 Torr), τ_{Loss}^O changes only slightly with increasing RF power and pressure. If assuming that $O(^3P)$ is lost only on the wall and to estimate the corresponding loss time as $\tau_w^O \approx 2R/(\gamma_O v_{\text{th}})$, one can obtain $\tau_w^O > \tau_{\text{Loss}}^O$ and, moreover, another dependence on RF power will take place. This indirectly confirms that volume losses of oxygen atoms play an important role.

First of all, it should be noted that gas heating is high enough under the studied conditions due to high specific RF power (up to 30 W cm^{-3}). The gas temperature in the tube is so high that it provides very fast decomposition of ozone (mainly in collisions with both O_2 and $O(^3P)$). Therefore, O_3 is present only in the cold area near the wall. It is clearly demonstrated

by figure 8 where examples of O_3 radial profiles are shown. The thickness of the O_3 layer is less than 1 mm since ozone diffusing to the tube center is quickly decomposed back to $O(^3P)$ and O_2 . It effectively excludes the three-body reaction of O_3 production from the possible $O(^3P)$ loss processes.

Thus, only reactions that lead to products being stable at high temperatures can influence the $O(^3P)$ loss. The one stable product chemically differing from O and O_3 is the O_2 molecule. Therefore, there are only two possible reactions of O atom loss:

- (i) reaction of $O(^3P)$ atoms with ozone producing two O_2 molecules (see section 1, reaction (I.4)) and
- (ii) three-body recombination of $O(^3P)$ atoms into O_2 (see Introduction, reaction (I.5)).

Radial profiles of the O atom loss rates (ν_{Loss}) were estimated for each of the processes (I.4) and (I.5) assuming local approximation and using radial density distributions of $O(^3P)$ atoms as well as O_3 and O_2 molecules. An example of such estimation is shown in figure 13. The thick green line marks the value of the total loss rate obtained by the time-resolved actinometry. It can be seen that three-body recombination is the dominant O atom volume loss process and near the wall it becomes comparable with ν_{Loss} from time-resolved actinometry. In the central area of the discharge, where the gas temperature is high enough, the volume loss rate is rather low. So, oxygen atoms produced there only have the possibility to diffuse toward the wall and to recombine either in the thin cold layer of gas near the wall or on the surface. Since increasing pressure limits the atom diffusion regardless, it allows for the accumulation of atoms and a high dissociation degree.

The ν_{Loss} estimation shows the importance of volume recombination for $O(^3P)$ atom loss, although it demonstrates the ‘surface character’ of this recombination since it occurs in the thin layer of gas near the wall. In some sense, it recalls the surface loss of oxygen atoms. Therefore, the characteristic

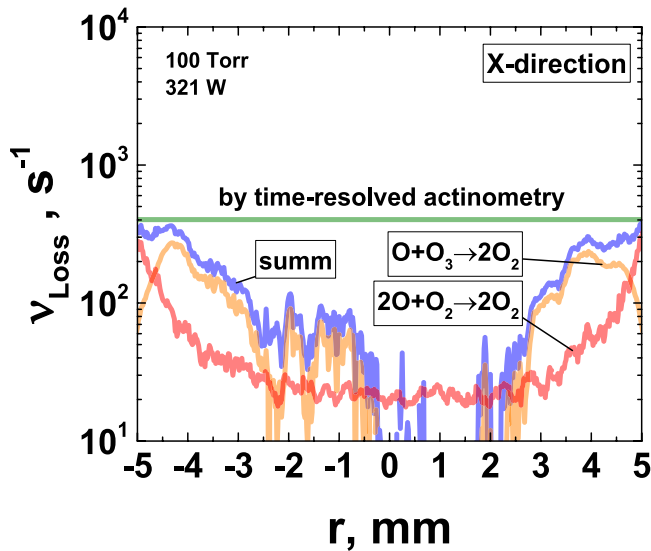


Figure 13. Example of radial profiles of the O atom loss rate estimated from the experimental profiles $T_{\text{gas}}(r)$, $[\text{O}^{(3)\text{P}}]/N(r)$ and $[\text{O}_3](r)$ in comparison with the result of time-resolved actinometry (thick green line).

$\text{O}^{(3)\text{P}}$ loss time was estimated according to the well-known approach (see [8] for example) from near-wall gradients of $[\text{O}^{(3)\text{P}}]/N$ radial profiles obtained by spatially resolved actinometry:

$$\tau_{\text{Loss}}^{\text{O}} \approx \frac{R \cdot [\text{O}]_{\text{nw}}/N}{2D_{\text{O}} \cdot \text{grad}_r([\text{O}]_{\text{nw}}/N)} \quad (15)$$

where R is the tube radius, D_{O} is the O atom diffusion coefficient in O_2 ($D_{\text{O}} \approx \frac{210}{P[\text{Torr}]} \cdot \left(\frac{T_{\text{gas}}[\text{K}]}{273}\right)^{1.77}$) and $[\text{O}]_{\text{nw}}$ is the O atom density near the wall. Results obtained according to (15) are shown by the symbols in figure 12(b) as a function of input RF power for different pressures. Similarly, figure 12(a) presents $\tau_{\text{Loss}}^{\text{O}}$ data obtained by time-resolved actinometry. Comparison of figures 12(a) and (b) shows a noticeable difference in $\tau_{\text{Loss}}^{\text{O}}$ data with the difference increasing with reducing pressure and increasing input RF power.

The total loss rate and loss time of O atoms were also calculated using the surface model (described in section 4.3) and the data on $\text{O}^{(3)\text{P}}$, O_3 densities and the gas temperature. The main goal of these calculations was analysis of the experimental data, which is why smooth approximations of the radial profiles were used in the model to exclude experimental noise.

The $\tau_{\text{Loss}}^{\text{O}}$ model calculations are shown in figures 12(a) and (b) by solid lines. It can be seen in figure 12(a) that simple analysis including $\text{O}^{(3)\text{P}}$ surface and volume recombination together reproduces $\text{O}^{(3)\text{P}}$ loss time data obtained by time-resolved actinometry quite well both in absolute value and in its variation with RF power and pressure. It is important to note that either surface or volume recombination solely do not allow one to fit experimental data on $\tau_{\text{Loss}}^{\text{O}}$. The contribution of both surface and volume recombination appears to be important. At lower pressures (<20 Torr) surface recombination somewhat prevails over the volume recombination (up to ~60%–65%) while as the pressure increases, the volume

recombination slowly starts to be dominant. Despite high pressure (60–100 Torr) and high $\text{O}^{(3)\text{P}}$ density, the surface recombination contribution is still not negligible due to noticeable gas heating near the wall. If one could support discharge at low RF power (~50–100 W) at the high pressures, the volume recombination would actually be dominant because of the gas temperature decrease. However, it is known that the CW RF discharges under similar conditions exist in the stable mode of so-called ‘normal current density’ below which the discharge is extinguished [54, 55]. Therefore, with decreasing RF power we observed the proportional decrease of the discharge length. Thus, to provide approximately the same conditions at each pressure the discharge was always maintained along the entire tube length, and it automatically established the minimal RF power for which it was possible.

As can be seen in figure 12(b), $\tau_{\text{Loss}}^{\text{O}}$ values estimated from spatial profiles of $[\text{O}^{(3)\text{P}}]/N$ agree with the calculations and data of time-resolved actinometry only for low RF powers and high pressures when distortions of the profiles induced by the plasma sheath influence are minimal (see figure 5(b)). With further RF power increase and, correspondingly, plasma sheath influence, the systematic discrepancy with the calculations and the time-resolved actinometry data also increases. Although this influence was taken into account by using actinometry of Kr and Ar atoms, it is quite possible that this accounting was not absolutely exact, leading to some systematic underestimation of the $[\text{O}^{(3)\text{P}}]/N$ gradients near the wall. In addition, it was rather difficult to measure accurately these gradients since the length, where it should be done (~0.5 mm) was already comparable with the spatial resolution of the used optical scheme. Nevertheless, at the lowest RF powers, when both the distortions and gradients of $[\text{O}^{(3)\text{P}}]/N$ profiles were small, the results of the space-resolved actinometry confirm the results of the time-resolved actinometry and of the surface model.

5. Conclusion

In this work, study of $\text{O}^{(3)\text{P}}$ atom loss in O_2 RF plasma has been carried out at an intermediate range of pressures (10–100 Torr) and input RF powers when the transition from the surface to volume loss should be observed. The research has shown that such a transition actually takes place. However, the study has also revealed the significant role of the gas temperature in this transition.

Firstly, it concerns rather high gas temperature (>1200 K) in plasma volume due to high values of specific RF power input because of the ‘normal current density’ effect. This leads to significant decrease of $\text{O}^{(3)\text{P}}$ loss rate in the discharge volume since O atom loss is limited by recombination on the surface and in the volume (in the thin layer of gas near the wall). The integral loss rate appears to be relatively low and provides a high dissociation degree of oxygen, i.e. a high $[\text{O}^{(3)\text{P}}]/N$ ratio. Thus, it supports the high flux of O atoms toward the tube wall.

Secondly, high values of specific RF power input also lead to increasing both gas temperature near the wall (because the

accommodation coefficient is less than unity) and temperature of the internal tube surface. This increases the O atom surface loss rate and simultaneously decreases the volume loss rate in front of the wall. The joint effect is that contributions of both volume and surface recombination of $O(^3P)$ atoms are important and should be taken into account.

Contributions of surface and volume recombination into $O(^3P)$ loss under the studied conditions were estimated and analyzed basing on the $O(^3P)$ surface loss model from [17] and the measured radial profiles of $[O(^3P)]/N$, T_{gas} and O_3 . The analysis confirmed the importance of both surface and volume losses. At a high O atom density near the wall, three-body recombination is the main loss channel for O atoms while recombination with physisorbed O atoms is the main surface loss channel.

Overall, $O(^3P)$ loss kinetics at intermediate pressures appears to be a rather complex phenomenon and requires 1D or even 2D modeling as a minimum for its correct description. Thus, the use of global models under similar conditions can lead to dubious results in detailed study of kinetic mechanisms and processes, while they can be still useful for simple analysis of experimental results.

Acknowledgments

The research was conducted in the scope of the KaPPA International Associated Laboratory (LIA). This research is supported by Russian Foundation for Basic Research (RFBR) Grant Nos. 16-52-16024 and 18-32-00932\18.

ORCID iDs

A V Volynets  <https://orcid.org/0000-0003-4893-7647>
 D V Lopaev  <https://orcid.org/0000-0003-4975-3487>
 S M Zyryanov  <https://orcid.org/0000-0003-1438-3631>
 M A Bogdanova  <https://orcid.org/0000-0001-6694-6032>
 A T Rakhimov  <https://orcid.org/0000-0001-5836-9319>

References

- [1] Cacciatore M, Rutigliano M and Billing G D 1999 Eley–Rideal and Langmuir–Hinshelwood recombination coefficients for oxygen on silica surfaces *J. Thermophys. Heat Transf.* **13** 195–203
- [2] Cacciatore M 1999 Some fundamental aspects of elementary gas-surface interactions *Pure Appl. Chem.* **71** 1809–17
- [3] Cacciatore M and Rutigliano M 2009 Dynamics of plasma-surface processes: E–R and L–H atom recombination reactions *Plasma Sources Sci. Technol.* **18** 023002
- [4] Gordiets B, Ferreira C M, Nahorny J, Pagnon D, Touzeau M and Vialle M 1996 Surface kinetics of N and O atoms in discharges *J. Phys. D: Appl. Phys.* **29** 1021–31
- [5] Kim Y C and Boudart M 1991 Recombination of oxygen, nitrogen, and hydrogen atoms on silica: kinetics and mechanism *Langmuir* **7** 2999–3005
- [6] Cartry G, Magne L and Cernogora G 2000 Atomic oxygen recombination on fused silica: modelling and comparison to low-temperature experiments (300 K) *J. Phys. D: Appl. Phys.* **33** 1303
- [7] Krištof J, Macko P and Veis P 2012 Surface loss probability of atomic oxygen *Vacuum* **86** 614–9
- [8] Lopaev D V, Malykhin E M and Zyryanov S M 2011 Surface recombination of oxygen atoms in O_2 plasma at increased pressure: I. The recombination probability and phenomenological model of surface processes *J. Phys. D: Appl. Phys.* **44** 015201
- [9] Guerra V 2007 Analytical model of heterogeneous atomic recombination on silicalike surfaces *IEEE Trans. Plasma Sci.* **35** 1397–412
- [10] Guerra V and Marinov D 2016 Dynamical Monte Carlo methods for plasma-surface reactions *Plasma Sources Sci. Technol.* **25** 45001
- [11] Macko P, Veis P and Cernogora G 2004 Study of oxygen atom recombination on a Pyrex surface at different wall temperatures by means of time-resolved actinometry in a double pulse discharge technique *Plasma Sources Sci. Technol.* **13** 251–62
- [12] Catry G, Magne L and Cernogora G 1999 Atomic oxygen recombination on fused silica: experimental evidence of the surface state influence *J. Phys. D: Appl. Phys.* **32** L53
- [13] Guerra V and Loureiro J 2004 Dynamical Monte Carlo simulation of surface atomic recombination *Plasma Sources Sci. Technol.* **13** 85–94
- [14] Marinov D, Teixeira C and Guerra V 2017 Deterministic and Monte Carlo methods for simulation of plasma-surface interactions *Plasma Process. Polym.* **14** 1–18
- [15] Guerra V, Marinov D, Guaitella O and Rousseau A 2014 NO oxidation on plasma pretreated Pyrex: the case for a distribution of reactivity of adsorbed O atoms *J. Phys. D: Appl. Phys.* **47** 224012
- [16] Tserepia A D and Miller T A 1995 Spatially and temporally resolved absolute O-atom concentrations in etching plasmas *J. Appl. Phys.* **77** 505
- [17] Booth J P, Guaitella O, Chatterjee A, Drag C, Guerra V L, Lopaev D V, Zyryanov S M, Rakhimova T V, Voloshin D G and Mankelevich Y A 2019 $O(^3P)$ atom recombination on a Pyrex surface in an O_2 plasma *Plasma Sources Sci. Technol.* **28** 055005
- [18] Steinfeld J I, Adler golden S M and Gallagher J W 1987 Critical survey of data on the spectroscopy and kinetics of ozone in the mesosphere and thermosphere *J. Phys. Chem. Ref. Data* **16** 911–51
- [19] Atkinson R, Baulch D L, Cox R A, Hampson R F, Kerr J A, Rossi M J and Troe J 1997 Evaluated kinetic, photochemical and heterogeneous data for atmospheric chemistry: supplement V. IUPAC subcommittee on gas kinetic data evaluation for atmospheric chemistry *J. Phys. Chem. Ref. Data* **26** 521–1011
- [20] Lin C L and Leu M T 1982 Temperature and third-body dependence of the rate constant for the reaction $O + O_2 + M \rightarrow O_3 + M$ *Int. J. Chem. Kinet.* **14** 417–34
- [21] Atkinson R, Baulch D L, Cox R A, Crowley J N, Hampson R F, Hynes R G, Jenkin M E, Rossi M J and Troe J 2004 Evaluated kinetic and photochemical data for atmospheric chemistry: volume I—gas phase reactions of O_x , HO_x , NO_x and SO_x species *Atmos. Chem. Phys.* **4** 1461–738
- [22] Young R A and Sharpless R L 1963 Chemiluminescent reactions involving atomic oxygen and nitrogen *J. Chem. Phys.* **39** 1071–102
- [23] Young R A and Black G 1966 Excited-state formation and destruction in mixtures of atomic oxygen and nitrogen *J. Chem. Phys.* **44** 3741–51
- [24] Patnaik A K, Adamovich I, Gord J R and Roy S 2017 Recent advances in ultrafast-laser-based spectroscopy and imaging for reacting plasmas and flames *Plasma Sources Sci. Technol.* **26** 103001
- [25] Šimek M 2014 Optical diagnostics of streamer discharges in atmospheric gases *J. Phys. D: Appl. Phys.* **47** 463001

- [26] Lukas C, Spaan M, Schulz-Von Der Gathen V, Thomson M, Wegst R, Döbele H F and Neiger M 2001 Dielectric barrier discharges with steep voltage rise: mapping of atomic nitrogen in single filaments measured by laser-induced fluorescence spectroscopy *Plasma Sources Sci. Technol.* **10** 445–50
- [27] Schmidt J B, Roy S, Sands B, Gord J R and Scofield J D 2017 Comparison of femtosecond- and induced fluorescence (TALIF) of atomic oxygen in atmospheric-pressure plasmas *Plasma Sources Sci. Technol.* **26** 055004
- [28] Volynets A V, Lopaev D V, Rakhimova T V, Chukalovsky A A, Mankelevich Y A, Popov N A, Zotovich A I and Rakhimov A T 2018 N₂ dissociation and kinetics of N (⁴S) atoms in nitrogen DC glow discharge *J. Phys. D: Appl. Phys.* **51** 364002
- [29] Melin G A and Madix R J 1971 Energy accommodation during oxygen atom recombination on metal surfaces *Trans. Faraday Soc.* **67** 198–211
- [30] Zyryanov S M and Lopaev D V 2007 Measurements of the gas temperature in an oxygen plasma by spectroscopy of the transition *Plasma Phys. Rep.* **33** 510–20
- [31] Macko P and Veis P 1999 Time resolved rotational temperature measurements in a low-pressure oxygen pulsed discharge. Simple and quick method for temperature determination *J. Phys. D: Appl. Phys.* **32** 246–50
- [32] Touzeau M, Vialle M, Zellagui a, Gousset G, Lefebvre M and Pealat M 2000 Spectroscopic temperature measurements in oxygen discharges *J. Phys. D: Appl. Phys.* **24** 41–7
- [33] Hagelaar G J M and Pitchford L C 2005 Solving the Boltzmann equation to obtain electron transport coefficients and rate coefficients for fluid models *Plasma Sources Sci. Technol.* **14** 722–33
- [34] Kramida A, Ralchenko Y, Reader J and Team N A 2018 *NIST Atomic Spectra Database (ver. 5.3)* (Gaithersburg, MD: National Institute of Standards and Technology)
- [35] Niemi K, Schultz-von der Gathen V and Döbele H F 2001 Absolute calibration of atomic density measurements by laser-induced fluorescence spectroscopy with two-photon excitation *J. Phys. D: Appl. Phys.* **34** 2330–5
- [36] Döbele H F, Mosbach T, Niemi K and Schulz-Von Der Gathen V 2005 Laser-induced fluorescence measurements of absolute atomic densities: concepts and limitations *Plasma Sources Sci. Technol.* **14** S31
- [37] Niemi K, Schulz-Von Der Gathen V and Döbele H F 2005 Absolute atomic oxygen density measurements by two-photon absorption laser-induced fluorescence spectroscopy in an RF-excited atmospheric pressure plasma jet *Plasma Sources Sci. Technol.* **14** 375–86
- [38] Belikov A E, Kusnetsov O V and Sharafutdinov R G 1995 The rate of collisional quenching of N₂O⁺ (B₂Σ), (B₂Σ), (b⁴Σ), O⁺ (3d), O (3p), Ar⁺ (4p'), Ar (4p,4p') at the temperature ≤200 K *J. Chem. Phys.* **102** 2792–801
- [39] Sadeghi N, Setser D W, Francis A, Czarnetzki U and Döbele H F 2001 Quenching rate constants for reactions of Ar(4p' [1/2]₀, 4p[1/2]₀, 4p[3/2]₂, and 4p[5/2]₂) atoms with 22 reagent gases *J. Chem. Phys.* **115** 3144–54
- [40] Hsu A G, Narayanaswamy V, Clemens N T and Frank J H 2011 Mixture fraction imaging in turbulent non-premixed flames with two-photon LIF of krypton *Proc. Combust. Inst.* **33** 759–66
- [41] Tayal S S and Zatsarinny O 2016 B-spline R-matrix-with-pseudostates approach for excitation and ionization of atomic oxygen by electron collisions *Phys. Rev. A* **94** 042707
- [42] Russ R, Gilmore F R and Rey M 1990 Updated excitation and ionization cross sections for electron impact on atomic oxygen *J. Phys. Chem. Ref. Data* **19** 277–305
- [43] Chilton J E, Boffard J B, Schappe R S and Lin C C 1998 Measurement of electron-impact excitation into the 3p⁵4p levels of argon using Fourier-transform spectroscopy *Phys. Rev. A* **57** 267–77
- [44] Chilton J E, Stewart M D and Lin C C 2000 Cross sections for electron-impact excitation of krypton *Phys. Rev. A* **62** 032714
- [45] Lopaev D V, Volynets A V, Zyryanov S M, Zotovich A I and Rakhimov A T 2017 Actinometry of O, N and F atoms *J. Phys. D: Appl. Phys.* **50** 075202
- [46] Ivanov V V, Klopovskii K S, Lopaev D V V, Rakhimov A T T, Rakhimova T V V, Klopovskii K S, Lopaev D V V, Rakhimov A T T and Rakhimova T V V 2000 Nonlocal nature of the electron energy spectrum in a glow-discharge in pure O₂: II. Actinometry of O(³P) atoms in a plasma at low gas pressures *Plasma Phys. Rep.* **26** 980–90
- [47] Lopaev D V and Smirnov A V 2004 Diagnostics of heterogeneous processes with the participation of radicals by time-resolved actinometry *Plasma Phys. Rep.* **30** 882–93
- [48] Okabe H 1978 *Photochemistry of Small Molecules* vol 431 (New York: Wiley)
- [49] Lunin V V, Popovich M P and Tkachenko S N 1998 *Physical Chemistry of Ozone* (Moscow: Moscow State University Press)
- [50] Lopaev D V, Malykhin E M and Zyryanov S M 2011 Surface recombination of oxygen atoms in O₂ plasma at increased pressure: II. Vibrational temperature and surface production of ozone *J. Phys. D: Appl. Phys.* **44** 015202
- [51] Marinov D, Guerra V, Guaitella O, Booth J-P and Rousseau A 2013 Ozone kinetics in low-pressure discharges: vibrationally excited ozone and molecule formation on surfaces *Plasma Sources Sci. Technol.* **22** 055018
- [52] Marinov D, Guaitella O, Booth J P and Rousseau A 2013 Direct observation of ozone formation on SiO₂ surfaces in O₂ discharges *J. Phys. D: Appl. Phys.* **46** 464013
- [53] Pagnon D, Amorim J, Nahorny J, Touzeau M and Vialle M 1995 On the use of actinometry to measure the dissociation in O₂ DC glow discharges: determination of the wall recombination probability *J. Phys. D: Appl. Phys.* **28** 1856–68
- [54] Raizer Y P, Shneider M N and Yatsenko N A 2017 *Radio-Frequency Capacitive Discharges* (Boca Raton, FL: CRC Press)
- [55] Braginskiy O V, Vasilieva A N, Klopovskiy K S, Kovalev A S, Lopaev D V, Proshina O V, Rakhimova T V and Rakhimov A T 2005 Singlet oxygen generation in O₂ flow excited by RF discharge: I. Homogeneous discharge mode: α-mode *J. Phys. D: Appl. Phys.* **38** 3609–25